

See discussions, stats, and author profiles for this publication at: <https://www.researchgate.net/publication/236335759>

Emission–Decay Curves, Energy–Transfer and Effective–Refractive Index in Gd₂O₃:Eu³⁺ Nanorods

ARTICLE *in* THE JOURNAL OF PHYSICAL CHEMISTRY C · JUNE 2011

Impact Factor: 4.77 · DOI: 10.1021/jp205093x

CITATIONS

28

READS

117

5 AUTHORS, INCLUDING:



Mengistie L. Debasu

University of Aveiro

11 PUBLICATIONS 108 CITATIONS

SEE PROFILE



Andreia G Macedo

Federal Technological University of Paraná - ...

25 PUBLICATIONS 221 CITATIONS

SEE PROFILE



Joao Rocha

University of Aveiro

455 PUBLICATIONS 9,830 CITATIONS

SEE PROFILE



Luís D Carlos

University of Aveiro

483 PUBLICATIONS 9,774 CITATIONS

SEE PROFILE

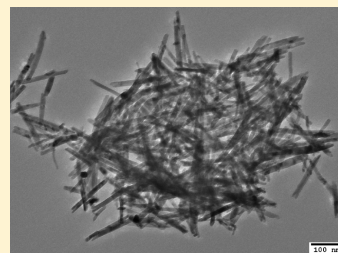
Emission-Decay Curves, Energy-Transfer and Effective-Refractive Index in $\text{Gd}_2\text{O}_3:\text{Eu}^{3+}$ Nanorods

Mengistie L. Debasu,^{†,‡} D. Ananias,[‡] Andreia G. Macedo,^{†,‡} J. Rocha,^{‡,*} and Luís D. Carlos^{†,*}

[†]Department of Physics and [‡]Department of Chemistry, CICECO, Universidade de Aveiro, 3810-193 Aveiro, Portugal

S Supporting Information

ABSTRACT: Cubic $\text{Gd}_2\text{O}_3:\text{Eu}^{3+}$ (0.30, 1.01, 2.78, and 4.60 mol %) nanorods with an average diameter of ca. 14 nm were synthesized at ambient pressure and mild temperature (70 °C), using a simple and cost-effective wet-chemical route. The emission-decay curves of the $^5\text{D}_1$ and $^5\text{D}_0$ levels, hereafter referred to as $^5\text{D}_1(\text{C}_2)$ and $^5\text{D}_0(\text{C}_2)$, were investigated. Although the decay time of the $^5\text{D}_0$ level of the Eu^{3+} ions residing in the C_2 site of cubic $\text{Gd}_2\text{O}_3:\text{Eu}^{3+}$ nanostructures were previously reported, little is known about the rise time component in the $^5\text{D}_0$ emission-decay curve and the energy-transfer pathways responsible for it. The $^5\text{D}_0(\text{C}_2)$ rise time and the $^5\text{D}_1(\text{C}_2)$ decay time exhibit similar and strong dependence on the Eu^{3+} concentration and temperature. The $^5\text{D}_1(\text{C}_2)$ decay time matches well the rise time extracted from the rising component of the $^5\text{D}_0(\text{C}_2)$ emission-decay curve. The decay time of the $^5\text{D}_0(\text{C}_2)$ level (ranging from 1.4 to 2.1 ms, depending on the filling factor of the nanorods) is longer than that of the bulk counterpart mainly due to the reduction in the size of the nanorods, which introduces an effective-refractive index smaller than the refractive index of Gd_2O_3 .



1. INTRODUCTION

There is a growing interest in the study of inorganic nanocrystals doped with trivalent lanthanide ions (Ln^{3+}) due to their wide range of industrial applications in areas such as electronic and photonic devices and amplification in optical communications,^{1–5} luminescent thermometers,^{6–8} fluorescent and magnetic resonance imaging,^{9–11} and biolabeling.^{12–15} For instance, red, green, blue and white-light emissions are generated from Ln^{3+} -doped Y_2O_3 nanocrystals excited using a low-cost commercial 980 nm laser diode.¹⁶ The first applications of $\text{Gd}_2\text{O}_3:\text{Eu}^{3+}$ nanoparticles as reporters in optical imaging of antibody micropatterns and fluorescent labels were reported by Nichkova et al.^{12,13} The same group also demonstrated a novel immunoassay using core-shell nanoparticles with magnetic cores of iron oxide doped with cobalt and neodymium, and $\text{Gd}_2\text{O}_3:\text{Eu}^{3+}$ luminescent shells.¹⁷ Recently, Das et al. reported Ln^{3+} -doped Gd_2O_3 nanorods as multimodal contrast agents for optical and magnetic resonance imaging.¹¹

In this context, understanding how the photoluminescent properties vary as a function of the size of the Ln^{3+} -doped nanocrystals (including nanotubes and nanorods) is an outstanding problem.^{18–28} In particular, when the size of the nanocrystals is much smaller than the wavelength of light, the radiative lifetime of the Ln^{3+} excited states is modified due to the change of the effective-refractive index and polarizability of the milieu surrounding the ions.^{25,27,28} The virtual-cavity and real-cavity models were widely employed to investigate the local-field effects on the spontaneous emission rate of an excited ion embedded in a dielectric medium.^{26,27,29} In nanocrystals, the phonon-confinement impacts the Ln^{3+} luminescence dynamics that depends on the low-energy phonon modes of the lattice. Such is the case of the anomalous thermalization of both, the $^7\text{F}_1 \rightarrow ^5\text{D}_1$ transition of $\text{Gd}_2\text{O}_3:\text{Eu}^{3+}$ nanotubes^{23,24} and Eu_2O_3

nanocrystals,²² and the $^2\text{H}_{11/2} \rightarrow ^4\text{I}_{15/2}$ upconversion transition of $\text{Gd}_2\text{O}_3:\text{Yb}^{3+},\text{Er}^{3+}$ nanotubes.²³ The phonon-confinement effects are mainly associated with the reduction in size of the host materials.

The synthesis conditions, such as concentration of dopant ions and calcination time and temperature, may change the Ln^{3+} radiative lifetimes and the mechanisms of energy-transfer between ions located in sites with different local symmetry.^{21,30–34} Among the inorganic oxides, Y_2O_3 and Gd_2O_3 were widely employed as ideal host materials for the Ln^{3+} down- or up-conversion emission because of their low-phonon energy, high chemical- and photostability, and efficient sensitization (host-to- Ln^{3+} energy transfer).^{14,16,17,21,23,24,30–41} In general, lanthanide sesquioxides, Ln_2O_3 , exhibit three main crystal structures, hexagonal, cubic, and monoclinic.^{31,33} Cubic Gd_2O_3 , for example, contains two nonequivalent cation sites, C_2 (noncentrosymmetric) and S_6 (centrosymmetric), in a 3:1 ratio.³¹ The Eu^{3+} energy levels of these two sites are, thus, quite different and energy-transfer occurs between them.^{23,24,31,35,36} For cubic $\text{Gd}_2\text{O}_3:\text{Eu}^{3+}$, which finds applications, e.g., in immunoassays,^{11–13,17,32} however, no analysis of the $^5\text{D}_1(\text{C}_2)$ and $^5\text{D}_0(\text{C}_2)$ emission-decay curves and energy-transfer mechanisms responsible for the rise-time component of the $^5\text{D}_0(\text{C}_2)$ emission-decay curve is available.^{32,34,35,37–40} In particular, evidence for the $^5\text{D}_0(\text{C}_2)$ rise time of $\text{Gd}_2\text{O}_3:\text{Eu}^{3+}$ nanotubes/nanorods is missing, though the $^5\text{D}_0(\text{C}_2)$ lifetime was reported.^{21,39}

Here, we center our attention on the $^5\text{D}_0(\text{C}_2)$ and $^5\text{D}_1(\text{C}_2)$ emission-decay curves of $\text{Gd}_2\text{O}_3:\text{Eu}^{3+}$ nanorods (Eu^{3+} concentration 0.30, 1.01, 2.78, and 4.60 mol %). The $^5\text{D}_1$ to $^5\text{D}_0$

Received: May 31, 2011

Revised: June 14, 2011

Published: June 30, 2011

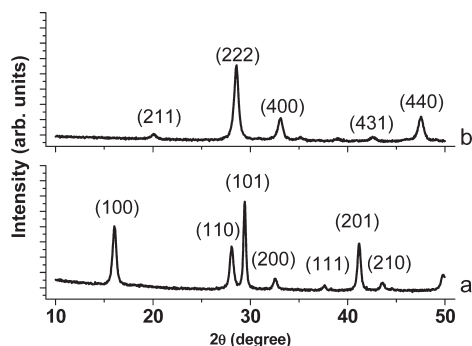


Figure 1. XRD patterns of (a) hexagonal $\text{Gd}(\text{OH})_3:2.78\% \text{Eu}^{3+}$ and (b) cubic $\text{Gd}_2\text{O}_3:2.78\% \text{Eu}^{3+}$ nanorods.

interlevel relaxation (or interlevel energy transfer) and the intersite energy-transfer pathways feeding the $^5\text{D}_0(\text{C}_2)$ level are investigated and the path responsible for the observed rise time in the $^5\text{D}_0(\text{C}_2)$ emission-decay curve is identified. The effects of the Eu^{3+} concentration and temperature on the $^5\text{D}_1(\text{C}_2)$ and $^5\text{D}_0(\text{C}_2)$ lifetimes are analyzed in detail. It is shown that the $^5\text{D}_0(\text{C}_2)$ lifetime is easily tuned by varying the dispersion/compactness of the nanorods in air, and this is attributed to the size of the nanorods and the effective-refractive index of the medium surrounding Eu^{3+} ions.

This work is a case study for understanding how in Ln^{3+} -containing nanostructures (interlevel and intersite) energy transfers that feed a given (emitting) energy level determine its lifetime, which, in turn, depends on the effective-refractive index and polarizability of the milieu surrounding the ions.

2. EXPERIMENTAL SECTION

2.1. Synthesis. $\text{Gd}_2\text{O}_3:\text{Eu}^{3+}$ nanorods with 0.30, 1.01, 2.78, and 4.60 mol % Eu^{3+} were synthesized by a simple wet-chemical route at low temperature and ambient pressure, following a modified procedure described in ref 39. In a typical synthesis of $\text{Gd}_2\text{O}_3:2.78\% \text{Eu}^{3+}$ nanorods, 9.00 mL of $\text{Gd}(\text{NO}_3)_3$ solution (0.4 M), and 0.560 mL of $\text{Eu}(\text{NO}_3)_3$ solution (0.2 M) were mixed with 40 mL distilled water in a 250 mL round-bottom flask. A 30-mL portion of NH_3 (25 wt %) was added to the mixture under magnetic stirring at room temperature. The resulting white solution was put in an ultrasonic bath for 3 min and then vigorously stirred again for 10 min at room temperature. The solution was then heated to 70 °C under continuous magnetic stirring for 16 h. After 16 h, the temperature was turned off and the solution was allowed to cool down to room temperature. The resulting white precipitate was washed several times with distilled water, once with ethanol and finally centrifuged and dried in air at 75 °C for 24 h, yielding $\text{Gd}(\text{OH})_3:\text{Eu}^{3+}$ powder. This powder was ground in an agate mortar to obtain relatively fine powder few milligrams of which were then calcined at 700 °C for 3 h, with heating and cooling rates of 5 °C/min, affording $\text{Gd}_2\text{O}_3:\text{Eu}^{3+}$ powder.

2.2. Measurements. The Eu^{3+} and Gd^{3+} contents of the calcined $\text{Gd}_2\text{O}_3:\text{Eu}^{3+}$ powders were determined by inductively coupled plasma atomic emission spectroscopy (ICP-AES) analysis. The powder X-ray diffraction (XRD) patterns of the dried and calcined powder samples were collected on a Philips X'Pert MPD Powder X-ray Diffractometer ($\text{CuK}\alpha$ radiation at 1.54 Å) in the 2θ range between 10 and 50°, with a 0.04° step scan mode.

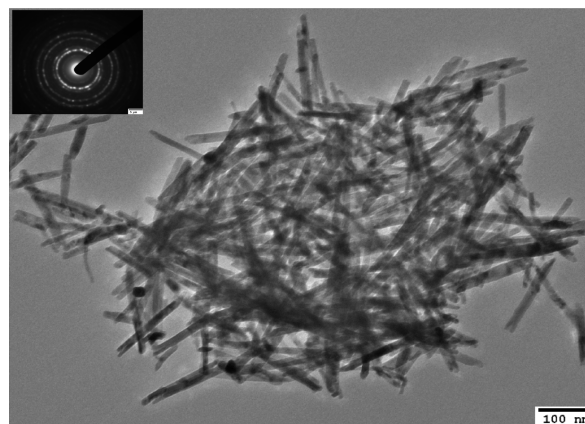


Figure 2. TEM image of $\text{Gd}_2\text{O}_3:2.78\% \text{Eu}^{3+}$ nanorods. The inset shows the electron-diffraction pattern.

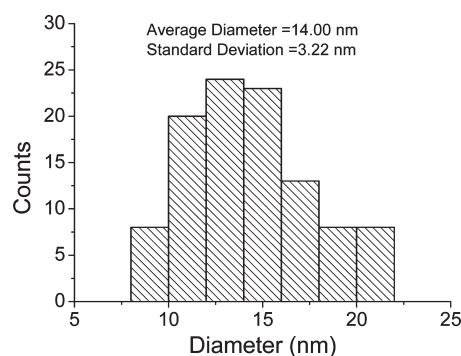


Figure 3. Size distribution of the nanorods shown in Figure 2.

The morphology of the calcined samples was analyzed on Hitachi SU-70 scanning electron microscope in the transmission mode (STEM) (Figure S2 of the Supporting Information, SI) and Hitachi H9000-NA transmission electron microscope (TEM). The emission and excitation spectra were recorded at 11 and 300 K using a Fluorolog-3 Horiba Scientific (Model FL3-2T) spectroscopy, with a modular double grating excitation spectrometer (fitted with a 1200 grooves/mm grating blazed at 330 nm) and a TRIAX 320 single emission monochromator (fitted with a 1200 grooves/mm grating blazed at 500 nm, reciprocal linear density of 2.6 $\text{nm} \cdot \text{mm}^{-1}$), coupled to a R928 Hamamatsu photomultiplier, using the front face acquisition mode. The excitation source was a 450 W Xe arc lamp. The emission spectra were corrected for detection and optical spectral response of the spectrofluorimeter and the excitation spectra were corrected for the spectral distribution of the lamp intensity using a photodiode reference detector. Time-resolved measurements were carried out with the setup described for the luminescence spectra using a pulsed Xe—Hg lamp (6 μs pulse at half width and 20–30 μs tail). The measurements were performed using a helium-closed cycle cryostat with vacuum system measuring $\sim 10^{-6}$ mbar and the temperature was increased in steps of 10 K using a Lakeshore 330 autotuning temperature controller with a resistance heater. A small amount of the calcined nanorods was dispersed on a copper plate covered with vacuum grease. The powder was then slightly compacted against the plate to confirm that it would be stable during the measurement. For the purpose of observing the filling factor effects, powder pellets were prepared under a hydraulic press.

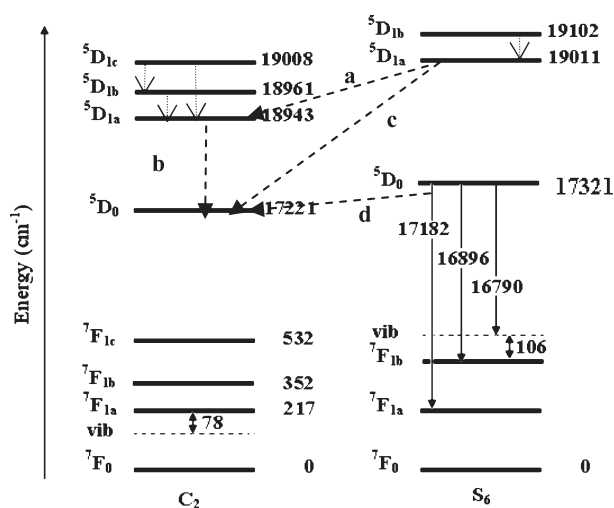


Figure 4. Partial Eu^{3+} energy-level diagram for the C_2 and S_6 sites in cubic $\text{Gd}_2\text{O}_3:\text{Eu}^{3+}$ nanotubes/nanorods (error ca. 10 cm^{-1}).²³ Transitions a, c, and d represent intersite energy-transfer, whereas transition b stands for interlevel relaxation.^{7,30}

3. RESULTS AND DISCUSSION

The nominal concentrations of 0.30, 1.00, 3.00, and 5.00 mol % Eu^{3+} relative to Gd^{3+} in the starting materials were found to be, in fact, 0.30, 1.01, 2.78, and 4.60 mol % Eu^{3+} , respectively, in the final $\text{Gd}_2\text{O}_3:\text{Eu}^{3+}$ nanorods. The XRD peaks of all samples before calcination are indexed into the pure hexagonal $\text{Gd}(\text{OH})_3$ phase (PDF file: PDF-083–2037). Figure 1 shows the diffraction patterns of $\text{Gd}(\text{OH})_3:2.78\% \text{Eu}^{3+}$ and $\text{Gd}_2\text{O}_3:2.78\% \text{Eu}^{3+}$ nanorods obtained after calcination at 700°C for 3 h. All calcined samples correspond to the pure Gd_2O_3 cubic phase, according to PDF-004-8970 and ref 39. The XRD patterns of all remaining samples are given in Figure S1 of the SI. TEM images show that the nanorods are relatively uniform in diameter and length (Figure 2), while the electron-diffraction patterns indicate that they are polycrystalline. As shown in Figure 3, the size distribution for 105 nanorods ranges from 10 to 20 nm, with an average diameter of 14 nm, which is much smaller than the diameter of the nanotubes reported by Jia et al.³⁹ The length of the nanorods is smaller than 180 nm.

3.1. $^5\text{D}_{0,1}(\text{C}_2)$ Rise Time and Decay Time. The emission-decay curves of the $^5\text{D}_0(\text{C}_2)$ and $^5\text{D}_1(\text{C}_2)$ levels were recorded after a 0.01 ms initial delay of the excitation pulse by monitoring the emission within the $^5\text{D}_0 \rightarrow ^7\text{F}_2(\text{C}_2)$ transition at 610.7 nm and the $^5\text{D}_1 \rightarrow ^7\text{F}_1(\text{C}_2)$ transition at 534 nm, respectively, using an excitation wavelength of 260 nm (within the ligand-to-metal charge-transfer band²⁵). Since the emission and excitation spectra (Figures S3 and S4 of the SI) of Eu^{3+} in cubic Gd_2O_3 have been discussed elsewhere,^{23,24,31,36} only the spectral features and electronic-energy levels relevant to the study of the rise time, decay time and energy-transfer processes are presented here. Additional evidence is given in the SI.

Figure 4 shows a schematic representation of the $^5\text{D}_1(\text{C}_2)$ to $^5\text{D}_0(\text{C}_2)$ interlevel and $^5\text{D}_{1,0}(\text{S}_6)$ to $^5\text{D}_{1,0}(\text{C}_2)$ intersite energy-transfer processes in cubic $\text{Gd}_2\text{O}_3:\text{Eu}^{3+}$. Under 260 nm excitation, electrons from the C_2 and S_6 ground states are excited to higher-energy states, including the $^5\text{D}_1$ and $^5\text{D}_0$ levels. There are several energy-transfer channels that populate the lower $^5\text{D}_0(\text{C}_2)$ levels (Figure 4). Four energy-transfer pathways feeding the

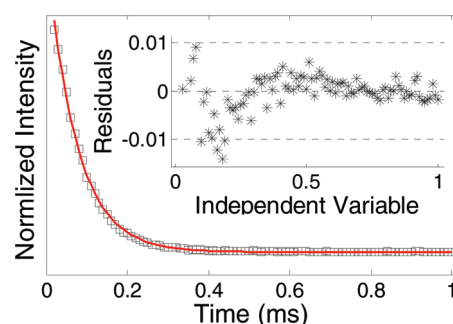


Figure 5. $^5\text{D}_1(\text{C}_2)$ emission-decay curve of $\text{Gd}_2\text{O}_3:2.78\% \text{Eu}^{3+}$ nanorods measured at 11 K, monitoring the emission at 534 nm and with excitation at 260 nm. The solid line is the fitting curve, the squares (\square) are the experimental data and the inset displays a plot of the residuals vs independent variable; the reduced χ -square and coefficient of determination are denoted $\chi^2_{\text{red}} = 5.44 \times 10^{-5}$ and $R^2 = 0.9986$, respectively.

$^5\text{D}_0(\text{C}_2)$ and/or $^5\text{D}_1(\text{C}_2)$ levels were considered to analyze the $^5\text{D}_0(\text{C}_2)$ and $^5\text{D}_1(\text{C}_2)$ emission-decay curves.

For all $\text{Gd}_2\text{O}_3:\text{Eu}^{3+}$ nanorods with 0.30–4.60 mol % Eu^{3+} , the $^5\text{D}_1(\text{C}_2)$ emission-decay curves (Figure S5 of the SI) measured at 11 and 300 K are well described by a single exponential, $n = n_0 \exp((-t)/(\tau_{D_1}))$, where n and n_0 are the number of electrons in the $^5\text{D}_1(\text{C}_2)$ level at time t and $t = 0$, respectively, and τ_{D_1} is the $^5\text{D}_1(\text{C}_2)$ decay time. Figure 5 shows a typical emission-decay curve of the $^5\text{D}_1(\text{C}_2)$ level. The residuals (inset in Figure 5) are randomly distributed around zero, indicating that the experimental data are well described by the model. The estimated decay times are collected in Table 1. The single-exponential character of the $^5\text{D}_1 \rightarrow ^7\text{F}_1(\text{C}_2)$ emission for Eu^{3+} in Y_2O_3 nanotubes/nanowires was also noted by Bai et al.⁴¹

The behavior of the $^5\text{D}_1(\text{C}_2)$ emission-decay curve confirms that all the interlevel and intersite energy-transfers feeding the $^5\text{D}_1(\text{C}_2)$ level are much faster than the $^5\text{D}_1(\text{C}_2)$ decay time. The presence of a relatively long-lived feeding level would cause the $^5\text{D}_1(\text{C}_2)$ emission-decay curve to have a rising component.⁶ In fact, the energy-transfer from the $^5\text{D}_1(\text{S}_6)$ to the $^5\text{D}_{1,0}(\text{C}_2)$ levels, achieved along path a and/or c in Figure 4, is witnessed by the appearance of the $^7\text{F}_0 \rightarrow ^5\text{D}_{1a,b}(\text{S}_6)$ transitions at 11 and 300 K in the steady-state excitation spectra acquired by monitoring the $^5\text{D}_0 \rightarrow ^7\text{F}_2(\text{C}_2)$ emission at 610.7 nm (Figure S4 of the SI). Therefore, as the $^5\text{D}_1(\text{C}_2)$ emission-decay curve exhibits no rising component, the observed energy-transfer to the $^5\text{D}_1(\text{C}_2)$ level along path a is much faster than the $^5\text{D}_1(\text{C}_2)$ decay time.

To clarify the nature of energy-transfer along paths b, c, and d we now discuss the behavior of the $^5\text{D}_0(\text{C}_2)$ emission-decay curve. This curve exhibits a rising part before decaying (similar to the curve in Figure 6), indicating that there is a decaying source feeding this level. The $^5\text{D}_0(\text{C}_2)$ decay curve is well described by a simplified model equation:⁷

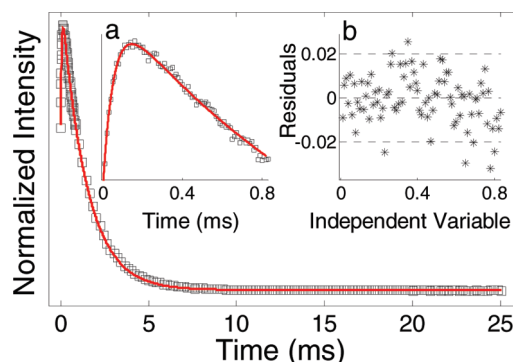
$$N = \left[N_0 + N_1 \left(1 - \exp\left(\frac{-t}{\tau_{rs}}\right) \right) \right] \exp\left(\frac{-t}{\tau_{D_0}}\right) \quad (1)$$

where N and N_0 are, respectively, the number of electrons in the $^5\text{D}_0(\text{C}_2)$ level at time t and $t = 0$; N_1 is the number of electrons at $t = 0$ in an upper feeding level; τ_{rs} and τ_{D_0} are, respectively, the rise time and the decay time of the $^5\text{D}_0(\text{C}_2)$ level.

For all of the samples, the $^5\text{D}_0(\text{C}_2)$ emission-decay curves (Figure S6 of the SI) acquired at 11 and 300 K were fitted with eq 1 using MATLAB routines and the obtained lifetimes are

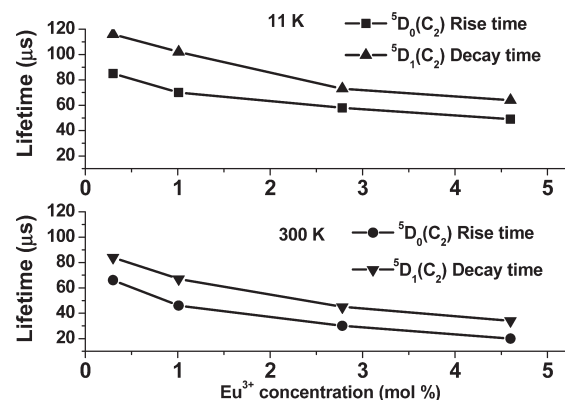
Table 1. $^5\text{D}_{0,1}(\text{C}_2)$ Lifetimes and Filling Factors for $\text{Gd}_2\text{O}_3:\text{Eu}^{3+}$ Nanorods in Air (The Calcination Temperature Was 700 °C for 3 h)

| Eu^{3+} (mol %) | $^5\text{D}_0(\text{C}_2)$ | | | | $^5\text{D}_1(\text{C}_2)$ | | filling factor |
|--------------------------|----------------------------|--------------------------|--------------------------------------|--------------------------------------|---------------------------------------|---------------------------------------|----------------|
| | 11 K | | 300 K | | 11 K | 300 K | |
| | τ_{D_0} (ms) | τ_{D_0} (ms) | τ_{rs} (μs) | τ_{rs} (μs) | τ_{D_1} (μs) | τ_{D_1} (μs) | |
| 0.30 | 1.40 ± 0.015 | 1.42 ± 0.008 | 85 ± 1.81 | 66 ± 0.84 | 116 ± 1.30 | 84 ± 0.71 | 0.78 |
| 1.01 | 1.73 ± 0.015 | 1.75 ± 0.013 | 70 ± 1.46 | 46 ± 1.09 | 102 ± 2.49 | 67 ± 0.61 | 0.67 |
| 2.78 | 1.41 ± 0.009 | 1.56 ± 0.009 | 58 ± 1.30 | 31 ± 0.89 | 73 ± 1.40 | 45 ± 0.40 | 0.78 |
| 4.60 | 1.35 ± 0.007 | 1.46 ± 0.009 | 49 ± 1.33 | 20 ± 0.98 | 64 ± 1.35 | 35 ± 0.21 | 0.80 |

**Figure 6.** $^5\text{D}_0(\text{C}_2)$ emission-decay curve acquired at 11 K for $\text{Gd}_2\text{O}_3:2.78\% \text{Eu}^{3+}$ nanorods, monitoring the emission at 610.7 nm and with excitation at 260 nm. The solid line is the fitting curve from eq 1 and the squares (\square) are the experimental data; the reduced χ -square and coefficient of determination are denoted $\chi^2_{\text{red}} = 6.00 \times 10^{-5}$ and $R^2 = 0.9996$, respectively; a and b in the inset depict the rising component and plot of the residuals vs independent variable, respectively.

collected in Table 1. The graphical view of residuals (inset b in Figure 6) and the goodness of fit statistics indicate that the model equation describes well the experimental data. One example of $^5\text{D}_0(\text{C}_2)$ emission-decay curve is shown in Figure 6.

3.2. Effects of Concentration and Temperature. The estimated $^5\text{D}_1(\text{C}_2)$ decay time and the $^5\text{D}_0(\text{C}_2)$ rise time extracted from the rising component of the $^5\text{D}_0(\text{C}_2)$ emission-decay curve using eq 1 strongly depend on the Eu^{3+} concentration and temperature (Figure 7). Several interaction mechanisms including dipole–dipole, dipole–quadrupole, and exchange interactions, which depend on temperature, concentration and distance between the ions, were widely investigated.^{30,31,42} The effect of the Eu^{3+} concentration on the lifetimes could be explained in terms of these interactions. At a given temperature, increasing the Eu^{3+} concentration shortens the $^5\text{D}_1(\text{C}_2)$ decay time and the $^5\text{D}_0(\text{C}_2)$ rise time (Figure 7), which implies a back-energy transfer from the $^5\text{D}_1(\text{C}_2)$ to $^5\text{D}_1(\text{S}_6)$ and/or an energy-transfer from the $^5\text{D}_1(\text{C}_2)$ level to the quenching centers. Even though it cannot be confirmed from the excitation spectra as no emission can be monitored for the $^5\text{D}_1(\text{S}_6)$ level, the former hardly occurs at 11 K. The latter is, however, likely to happen at relatively high ($>0.1\%$) Eu^{3+} concentrations³¹ due to the presence of quenching centers, such as nanorods surface defects.^{21,33,41} As the Eu^{3+} concentration increases, the probability of energy migration from the Eu^{3+} ions in the C_2 sublattice to the quenching centers increases,^{31,42} thereby shortening the $^5\text{D}_1(\text{C}_2)$ decay time. Considering the 3:1 population ratio of the Eu^{3+} ions in the two sites, such energy migration over the C_2 sublattice is dominant.³¹ The

**Figure 7.** $^5\text{D}_0(\text{C}_2)$ rise time and $^5\text{D}_1(\text{C}_2)$ decay time of $\text{Gd}_2\text{O}_3:\text{Eu}^{3+}$ nanorods as a function of the Eu^{3+} concentration.

relative intensities of the $^5\text{D}_1 \rightarrow ^7\text{F}_1(\text{C}_2)$ emissions support such energy migration. The intensity of the $^5\text{D}_1 \rightarrow ^7\text{F}_1(\text{C}_2)$ emission at 11 and 300 K decreases with increasing Eu^{3+} concentration (Figure S7 of the SI), suggesting that energy migration due to concentration effect is the most likely mechanism responsible for shortening the $^5\text{D}_1(\text{C}_2)$ decay time. At higher Eu^{3+} concentration, the $^5\text{D}_0(\text{C}_2)$ rise time also shortens, and there is a stronger quenching of the rising intensity in the $^5\text{D}_0(\text{C}_2)$ emission-decay curve (Figure S6 of the SI). Moreover, the $^5\text{D}_1(\text{C}_2)$ decay time at 11 K is 116 μs for 0.30% and 64 μs for 4.60% Eu^{3+} concentration (Table 1). A similar observation of a decrease in the $^5\text{D}_1(\text{C}_2)$ decay time from 134 μs , for 0.02% Eu^{3+} , to 66 μs , for 5% Eu^{3+} , in bulk Y_2O_3 crystals was reported by Buijs et al.³¹

For a given Eu^{3+} concentration, the decrease in the $^5\text{D}_0(\text{C}_2)$ rise time and the $^5\text{D}_1(\text{C}_2)$ decay time from 11 to 300 K shows that they are also sensitive to temperature. According to the theory of multiphonon relaxation, as the energy gap between an emitting upper level and the next lower level becomes smaller, the decay time from the upper to the lower level decreases due to the involvement of phonon emissions.^{43,44} Considering the maximum phonon energy in bulk Gd_2O_3 ca. 600 cm^{-1} ,³⁶ nearly three phonons are emitted from the $^5\text{D}_1(\text{C}_2)$ to $^5\text{D}_0(\text{C}_2)$ level due to lattice vibrations at high temperature, thus shortening the $^5\text{D}_1(\text{C}_2)$ decay time. The $^5\text{D}_1(\text{C}_2)$ decay time at 300 K may also be shortened by energy migration,⁴² which increases with temperature, from the C_2 sublattice to the quenching centers. It should be noted that the $^5\text{D}_0(\text{C}_2)$ rise time is also influenced by temperature. Accordingly, the $^5\text{D}_1(\text{C}_2)$ decay times for $\text{Gd}_2\text{O}_3:4.60\% \text{Eu}^{3+}$ nanorods decrease from 64 μs , at 11 K, to 34 μs , at 300 K. These values are similar to those reported by Liu et al.³⁶ for 5% Eu^{3+} in Gd_2O_3 nanorods (65 μs , at 10 K, and 37 μs

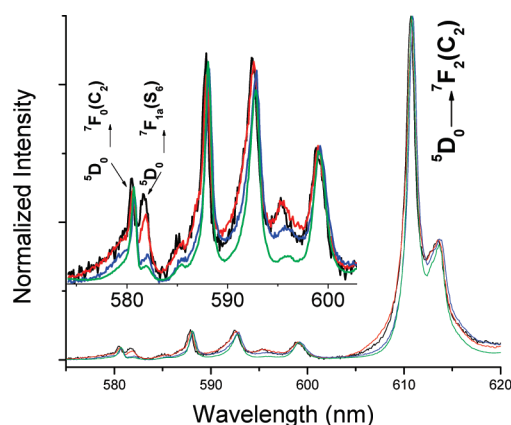


Figure 8. Emission spectra of $\text{Gd}_2\text{O}_3:\text{Eu}^{3+}$ nanorods at 11 K acquired under excitation at 260 nm and Eu^{3+} concentration 0.30% (black line), 1.01% (red), 2.78% (blue) and 4.60% (green). The inset depicts the relative intensity of the $^5\text{D}_0 \rightarrow ^7\text{F}_0(\text{C}_2)$ and $^5\text{D}_0 \rightarrow ^7\text{F}_{1a}(\text{S}_6)$ emissions, showing an efficient intersite energy transfer from the $^5\text{D}_0(\text{S}_6)$ to $^5\text{D}_0(\text{C}_2)$ level at high Eu^{3+} concentration.

at 295 K). The Eu^{3+} concentration seems to have no influence on the $^5\text{D}_0(\text{C}_2)$ decay time measured at a given temperature, that is, the effect of concentration quenching on the $^5\text{D}_0(\text{C}_2)$ decay time is negligible. Indeed, the energy gap between the $^5\text{D}_0$ and the $^7\text{F}_0$ levels is relatively large ($>12\,000\text{ cm}^{-1}$), which is not easily overcome by nonradiative processes induced by temperature and/or ion–ion interactions. The absence of a significant concentration effect on the $^5\text{D}_0(\text{C}_2)$ decay time was previously reported by Pires et al.³⁷ for 1–5% Eu^{3+} concentration in spherical Gd_2O_3 nanoparticles (although the rise time was not presented).

The $^5\text{D}_0(\text{C}_2)$ decay time of $\text{Gd}_2\text{O}_3:1.01\%\text{Eu}^{3+}$ nanorods was measured at temperatures in the range from 11 to 300 K and, as expected, the decay time hardly changed (Table S1 of the SI). The most pronounced effect on the $^5\text{D}_0(\text{C}_2)$ decay time is observed due to the change in the effective-refractive index (filling factor), which may be easily modified by changing the dispersion of the nanorods in air. A change in the dispersion of the nanorods in air during the measurement resulted in a significant variation of the $^5\text{D}_0(\text{C}_2)$ decay time. In general, the $^5\text{D}_0(\text{C}_2)$ decay times of all samples are longer than that of the bulk counterparts, 1.00 and 0.94 ms reported by Andreia et al.²³ and Liu et al.,³⁶ respectively, and agree with those previously reported results for analogous materials.^{21,23,32,37,40,41} The increase in the $^5\text{D}_0(\text{C}_2)$ decay time is attributed to the modification of the effective-refractive index of the medium surrounding the Eu^{3+} ions due to the reduction in the size of the nanorods.

Under excitation at 394 nm, the rise-time phenomena were also noticed in the $\text{Gd}_2\text{O}_3:\text{Eu}^{3+}$ nanocrystals prepared through a hydrothermal method by Andreia et al.²³ For comparison with the present samples, the $^5\text{D}_0(\text{C}_2)$ lifetimes of $\text{Gd}_2\text{O}_3:1.00\%\text{Eu}^{3+}$ nanotubes²³ were measured with excitation in the ligand–metal charge transfer band (Figure S8 of the SI). The $^5\text{D}_0(\text{C}_2)$ rise time (77 μs at 11 K and 47 μs at 300 K) and the $^5\text{D}_0(\text{C}_2)$ decay time (1.41 ms at 11 K and 1.57 ms at 300 K) are in agreement with the corresponding lifetimes measured for 1.01% Eu^{3+} in the nanorods (Table 1). As was mentioned, the small differences in the $^5\text{D}_0(\text{C}_2)$ decay times, however, may be associated with the differences in the dispersion of the nanotubes and nanorods in air.

3.3. Energy-Transfers and Rationalization of the Rise Time. In this section, (interlevel and intersite) energy-transfer along paths *b*, *c*, and *d* in Figure 4 are defined and the rise time is rationalized. First, the contribution of energy-transfer along path *d* to the rise time can be clearly identified from the emission and excitation spectra. In the steady-state emission spectra acquired under excitation at 260 nm, energy-transfer from the $^5\text{D}_0(\text{S}_6)$ to $^5\text{D}_0(\text{C}_2)$ level induced by Eu^{3+} concentration was detected at 11 K (inset in Figure 8) and 300 K (Figure S9 of the SI). At high Eu^{3+} concentration, the $^5\text{D}_0 \rightarrow ^7\text{F}_{1a}(\text{S}_6)$ emission intensity decreases whereas that of the $^5\text{D}_0 \rightarrow ^7\text{F}_0(\text{C}_2)$ emission increases at the expenses of the $^5\text{D}_0 \rightarrow ^7\text{F}_{1a}(\text{S}_6)$ emission (Figure 8). In other words, a relatively efficient energy-transfer from the $^5\text{D}_0(\text{S}_6)$ to $^5\text{D}_0(\text{C}_2)$ level occurs at 11 K over an energy gap of ca. 100 cm^{-1} for the sample with the highest Eu^{3+} concentration. These results are similar to those reported by Zych for $\text{Lu}_2\text{O}_3:\text{Eu}^{3+45}$ and in agreement with Heber's et al.³⁰ empirical function for the dependence of the energy-transfer probability, $W_t \approx (1 - \exp(-c/c_0))$, between the two sites, where *c* and *c*₀ are the molar concentration of Eu^{3+} . No back energy-transfer from the $^5\text{D}_0(\text{C}_2)$ to $^5\text{D}_0(\text{S}_6)$ level was, however, observed as confirmed from the excitation spectra obtained by monitoring the $^5\text{D}_0 \rightarrow ^7\text{F}_{1a}(\text{S}_6)$ emission at 581.5 nm.³⁶ Therefore, if the rise time is due to an efficient energy-transfer from the $^5\text{D}_0(\text{S}_6)$ to $^5\text{D}_0(\text{C}_2)$ level, it must be relatively long for the sample having high Eu^{3+} content. This is, however, in contrast with Figure 7, which clearly shows a decrease in the rise time on increasing the Eu^{3+} concentration both at 11 and 300 K. The result proves that the $^5\text{D}_0(\text{C}_2)$ rise time does not arise due to the intersite energy-transfer from the $^5\text{D}_0(\text{S}_6)$ to $^5\text{D}_0(\text{C}_2)$ level, i.e., along path *d*, leading to the conclusion that the energy-transfer along path *d* is much faster than the $^5\text{D}_0(\text{C}_2)$ rise time, as the energy-transfer along path *a* was found to be too fast compared to the $^5\text{D}_1(\text{C}_2)$ decay time. Moreover, the energy-transfer along path *c* is obviously ruled out if one considers the small energy gap between the $^5\text{D}_1(\text{S}_6)$ and $^5\text{D}_1(\text{C}_2)$ levels (compared to that between the $^5\text{D}_1(\text{S}_6)$ and $^5\text{D}_0(\text{C}_2)$ levels). This implies that the observed energy-transfers from the $^5\text{D}_1(\text{S}_6)$ to $^5\text{D}_{1,0}(\text{C}_2)$ levels (Figure S4 of the SI) are preferably achieved only along path *a*. Additionally, the increase in the energy-transfer from the $^5\text{D}_1(\text{S}_6)$ to $^5\text{D}_{0,1}(\text{C}_2)$ levels on increasing Eu^{3+} concentration (Figure S4 of the SI) shows that the energy-transfer along path *c* is not responsible for the rise time, since the rise time shortens at high Eu^{3+} concentration (Figure 7). Finally, the interlevel relaxation along path *b* is the only route to slowly feed the $^5\text{D}_0(\text{C}_2)$ level. This can be deduced from the behaviors of the $^5\text{D}_1(\text{C}_2)$ decay time and the $^5\text{D}_0(\text{C}_2)$ rise time. The relatively long-lived emission of the $^5\text{D}_1(\text{C}_2)$ level suggests that the interlevel energy-transfer along path *b* may cause a rise time in the $^5\text{D}_0(\text{C}_2)$ emission-decay curve. As discussed above, the $^5\text{D}_0(\text{C}_2)$ rise time and $^5\text{D}_1(\text{C}_2)$ decay time follow a similar dependence as a function of the Eu^{3+} concentration and temperature (Figure 7 and Table 1). Furthermore, the $^5\text{D}_1(\text{C}_2)$ decay time matches the corresponding rise time component of the $^5\text{D}_0(\text{C}_2)$ emission-decay curve. The conclusion is that the main energy-transfer path responsible for the rise time in the $^5\text{D}_0(\text{C}_2)$ emission-decay curve is a direct relaxation from the $^5\text{D}_1(\text{C}_2)$ to the $^5\text{D}_0(\text{C}_2)$ level, path *b*. This is, however, in disagreement with the Ranson's et al.⁷ discussion of the rise time for the $\text{Y}_2\text{O}_3:\text{Eu}^{3+}$ phosphor, in which energy-transfer along paths *a*, *b*, and *d* were considered to be too fast ($<5\text{ }\mu\text{s}$) compared to the energy-transfer along path *c*, which was hold responsible for the rise time. In fact, the $\sim 5\text{ }\mu\text{s}$ rise time in the $^5\text{D}_0(\text{C}_2)$

Table 2. $^5\text{D}_0(\text{C}_2)$ Decay Times and Filling Factors of $\text{Gd}_2\text{O}_3:\text{Eu}^{3+}$ Nanorods in Different Pellet Forms in Air (the Calcination Temperature was 700 °C for 3 h)

| Eu^{3+} (mol %) | amount of powder (mg) | hydraulic press pressure | $^5\text{D}_0(\text{C}_2)$ decay time (ms) | filling factor |
|--------------------------|-----------------------|--------------------------|--|----------------|
| 0.30 | 200 | 7 ton | 1.45 ± 0.003 | 0.76 |
| | 20 | 2 ton | 1.94 ± 0.006 | 0.61 |
| | 10 | 1 ton | 2.10 ± 0.005 | 0.57 |

emission decay curve for the $\text{Y}_2\text{O}_3:\text{Eu}^{3+}$ phosphor was observed at a particular excitation wavelength (528.2 nm) by Hunt et al.⁴⁶ At 527.5 nm excitation wavelength, for instance, Hunt et al.⁴⁶ have also observed 200 μs $^5\text{D}_0(\text{C}_2)$ rise time for the same phosphor and they have pointed out that the emission-decay curves were strongly dependent on the excitation wavelengths.

3.4. Effective-Refractive Index and Filling Factor. As the average size of the nanorods (ca. 14 nm in diameter) is smaller than the irradiation wavelength, it is expected that the effective-refractive index and the polarizability of the medium surrounding the Eu^{3+} ions will be modified,^{25,27,28,47} thereby changing the radiative lifetime. A suitable theoretical model should be employed to describe this physical effect. Here, the virtual-cavity model was chosen because of its previous successful application to Ln^{3+} -doped oxide nanocrystals.^{25,26,35,36} By introducing a local-field correction factor according to the virtual-cavity model, the radiative lifetime, τ_{R} , of the emitting ion embedded in a medium with an effective-refractive index, n_{eff} , is given by the following:^{25,26}

$$\tau_{\text{R}} \approx \frac{\lambda_0^2}{f(\text{ED}) \left(\frac{1}{3}(n_{\text{eff}}^2 + 2) \right)^2 n_{\text{eff}}} \quad (2)$$

where λ_0 is the transition wavelength in vacuum; $f(\text{ED})$ is the electric-dipole oscillator strength of the transition and $n_{\text{eff}} = x n_{\text{Gd}_2\text{O}_3} + (1 - x) n_{\text{med}}$; x is the fraction of sample space occupied by the nanorods; $n_{\text{Gd}_2\text{O}_3}$ and n_{med} are the refractive indices of gadolinium oxide and the medium, respectively. We considered $n_{\text{Gd}_2\text{O}_3} = 1.976$,^{24,35} and $n_{\text{med}} = 1.0$.

The filling factor gives the fraction of sample volume occupied by the nanorods. Therefore, the larger the filling factor becomes, the greater the volume of sample occupied by the nanorods. In other words, in the limit $x = 1$, the effective-refractive index is that of the gadolinium oxide and thus the radiative lifetime of the nanorods will be close to that of the bulk counterparts. We noticed that the filling factor strongly depends on the compactness and dispersion of nanorods in air during the measurement and variation of the $^5\text{D}_0(\text{C}_2)$ decay time from 1.40 to 2.10 ms has been observed by simply changing the compactness and the dispersion of nanorods in air. For this purpose, e.g., 10 and 200 mg of $\text{Gd}_2\text{O}_3:0.30\% \text{Eu}^{3+}$ nanorods were prepared in the form of pellets with a hydraulic press under 2 and 7 tons, respectively, while keeping the other experimental conditions unchanged. The $^5\text{D}_0(\text{C}_2)$ decay time was 1.94 ms for the relatively thin pellet prepared at low pressure press, and 1.45 ms for the thick and highly compacted pellet (Table 2 and in Figure S10 of the SI). However, no significant change was observed in the $^5\text{D}_0(\text{C}_2)$ rise time (Table S2 of the SI). Even though further experimental studies are required, this effect may be qualitatively explained in terms of the filling factor of the nanorods and the change in the effective-refractive index, as pointed out by Meltzer et al.²⁵ Under high pressure press, the nanorods are obviously highly compacted

(no space between them and thus have high filling factor) and any local-field effect due to the reduction in size is lost. Instead, a highly compacted powder of nanorods behaves as the bulk counterpart.²⁸ On increasing the thickness and compactness of the powder pellet, the majority of the Eu^{3+} ions will be fully immersed in Gd_2O_3 and, hence, the effective-refractive index of the medium surrounding the emitters will be close to that of the Gd_2O_3 , leading to a shorter decay time. In addition, aggregates of nanorods larger than the wavelength of light do not show the local-field effect and the $^5\text{D}_0(\text{C}_2)$ decay time measured may become shorter than expected.^{26,28} This may explain why the filling factor (the $^5\text{D}_0(\text{C}_2)$ decay time) of the $\text{Gd}_2\text{O}_3:\text{Eu}^{3+}$ nanotubes was the same as that of the nanorods in ref 36 while the nanotubes were smaller in size.

Assuming that the $^5\text{D}_0 \rightarrow ^7\text{F}_2(\text{C}_2)$ transition is purely radiative, the filling factors of the nanorods from each sample were estimated using eq 2 and the results are summarized in Tables 1 and 2. As discussed, the filling factor depends on the dispersion of the nanorods in air. It ranges from 0.57 (for 2.10 ms) to 0.80 (for 1.35 ms). The result shows that the $^5\text{D}_0(\text{C}_2)$ decay time depends mainly on the dispersion of the nanorods in air and it is generally longer than that of the bulk counterpart. For analogous materials, Liu et al.^{35,36} have also observed a longer $^5\text{D}_0(\text{C}_2)$ decay time (2.20 ms) with a smaller estimated filling factor in air, 0.55, for $\text{Gd}_2\text{O}_3:5\% \text{Eu}^{3+}$ nanorods of 30–40 nm in diameter and 70–80 nm in length. Similarly, for $\text{Gd}_2\text{O}_3:\text{Eu}^{3+}$ nanotubes of 40 nm in diameter and 200–300 nm in length,³⁹ a 2.173 ms decay time was reported for the $^5\text{D}_0(\text{C}_2)$ level (no rise time observed). In order to compare experimental results, it is essential to describe the dispersion/suspension of the nanocrystals in a medium whenever the lifetime, effective-refractive index and filling factor are to be reported for nanocrystals smaller than the wavelength of light.

4. CONCLUSIONS

This work aimed at both understanding how in Ln^{3+} -containing nanostructures (interlevel and intersite) energy transfers that feed a given (emitting) energy level determine its lifetime and confirming that the latter depends on the effective-refractive index and polarizability of the milieu surrounding the ions. The control of the lifetime values is an important factor in the development of many applications of Ln^{3+} -doped nanostructures, such as, for instance, immunoassay purposes.

For this purpose, cubic phase $\text{Gd}_2\text{O}_3:0.30\text{--}4.60\% \text{Eu}^{3+}$ nanorods were prepared by a simple wet-chemical route at mild temperature and ambient pressure. The samples were characterized by XRD, ICP-AES, STEM, TEM, and PL. The $^5\text{D}_1(\text{C}_2)$ and $^5\text{D}_0(\text{C}_2)$ emission-decay curves were investigated in detail. The $^5\text{D}_1(\text{C}_2)$ emission-decay curve is described by a single exponential, whereas the $^5\text{D}_0(\text{C}_2)$ emission-decay curve comprises an initial rising component followed by an exponential tail. The $^5\text{D}_1(\text{C}_2)$ decay times match the corresponding rise times measured from the rising component of the $^5\text{D}_0(\text{C}_2)$ emission-decay

curve. Furthermore, the $^5\text{D}_1(\text{C}_2)$ decay time and the $^5\text{D}_0(\text{C}_2)$ rise time show similar behaviors upon changing the temperature and Eu^{3+} concentration. The $^5\text{D}_{0,1}(\text{S}_6)$ to $^5\text{D}_{0,1}(\text{C}_2)$ intersite energy-transfer is much faster than the $^5\text{D}_1(\text{C}_2)$ decay time and the $^5\text{D}_0(\text{C}_2)$ rise time. The contribution of the intersite energy-transfer mechanisms to the $^5\text{D}_0(\text{C}_2)$ rise time is ruled out, being the direct $^5\text{D}_1(\text{C}_2)$ to $^5\text{D}_0(\text{C}_2)$ relaxation (interlevel energy transfer) the only responsible path for the rise time effect. The longer $^5\text{D}_0(\text{C}_2)$ decay time observed for the nanorods (relatively to the bulk decay time) in air is mainly due to the small filling factor of the nanorods and the change in the effective-refractive index of the milieu surrounding the Eu^{3+} ions.

■ ASSOCIATED CONTENT

S Supporting Information. XRD patterns of the dried and calcined powder samples (Figure S1); STEM images of Gd_2O_3 : Eu^{3+} nanorods (Figure S2); emission and excitation spectra of the nanorods at 11 K (Figures S3 and S4); fitting curves of the $^5\text{D}_1(\text{C}_2)$ and $^5\text{D}_0(\text{C}_2)$ levels (Figures S5 and S6); emission spectra showing the relative intensity of the $^5\text{D}_1 \rightarrow ^7\text{F}_1(\text{C}_2)$ emissions at 11 and 300 K (Figure S7) and showing the energy transfer from the $^5\text{D}_0(\text{S}_6)$ to $^5\text{D}_0(\text{C}_2)$ level at 300 K (Figure S9); $^5\text{D}_0(\text{C}_2)$ emission decay curves of Gd_2O_3 :1.00% Eu^{3+} nanotubes (Figure S8); estimated $^5\text{D}_0(\text{C}_2)$ decay time for Gd_2O_3 :1.01% Eu^{3+} nanorods (Table S1), and the fitting curves of the $^5\text{D}_0(\text{C}_2)$ decay time for Gd_2O_3 :0.30% Eu^{3+} nanorods in the form of pellets prepared on a hydraulic press (Figure S10); $^5\text{D}_{1,0}(\text{C}_2)$ lifetimes and filling factors for Gd_2O_3 : Eu^{3+} nanorods in air (Table S2). This material is available free of charge via the Internet at <http://pubs.acs.org>.

■ AUTHOR INFORMATION

Corresponding Author

*E-mail: lcarlos@ua.pt (L.D.C.); rocha@ua.pt (J.R.).

■ ACKNOWLEDGMENT

We thank FCT for the financial support (Grant Reference SFRH/BD/67108/2009) and RNME-Pole University of Aveiro-FCT Project REDE/1509/RME/2005 for the access of STEM and TEM images. The help of RAS Ferreira (University of Aveiro, CICECO) in the time-resolved experiments is gratefully acknowledged.

■ REFERENCES

- Kar, A.; Patra, A. J. *Phys. Chem. C* **2009**, *113*, 4375.
- Sotiriou, G. A.; Schneider, M.; Pratsinis, S. E. *J. Phys. Chem. C* **2010**, *115*, 1084.
- Carlos, L. D.; Ferreira, R. A. S.; Bermudez, V. D.; Ribeiro, S. J. L. *Adv. Mater.* **2009**, *21*, 509.
- Xiao, Q.; Liu, Y.; Liu, L.; Li, R.; Luo, W.; Chen, X. *J. Phys. Chem. C* **2010**, *114*, 9314.
- Qu, X.; Song, H.; Pan, G.; Bai, X.; Dong, B.; Zhao, H.; Dai, Q.; Zhang, H.; Qin, R.; Lu, S. *J. Phys. Chem. C* **2009**, *113*, 5906.
- Chambers, M. D.; Clarke, D. R. *Annu. Rev. Mater. Res.* **2009**, *39*, 325.
- Ranson, R. M.; Evangelou, E.; Thomas, C. B. *Appl. Phys. Lett.* **1998**, *72*, 2663.
- Brites, C. D. S.; Lima, P. P.; Silva, N. J. O.; Millán, A.; Amaral, V. S.; Palacio, F.; Carlos, L. D. *Adv. Mater.* **2010**, *22*, 4499.
- Zhou, J.-C.; Sun, L.-D.; Shen, J.; Gu, J.-Q.; Yan, C.-H. *Nanoscale* **2011**, *3*, 1977.
- Bridot, J.-L.; Faure, A.-C.; Laurent, S.; Rivière, C.; Billotey, C.; Hiba, B.; Janier, M.; Josserand, V.; Coll, J.-L.; Vander Elst, L.; Muller, R.; Roux, S.; Perriat, P.; Tillement, O. *J. Am. Chem. Soc.* **2007**, *129*, 5076.
- Das, G. K.; Heng, B. C.; Ng, S.-C.; White, T.; Loo, J. S. C.; D'Silva, L.; Padmanabhan, P.; Bhakoo, K. K.; Selvan, S. T.; Tan, T. T. Y. *Langmuir* **2010**, *26*, 8959.
- Nichkova, M.; Dosev, D.; Gee, S. J.; Hammock, B. D.; Kennedy, I. M. *Anal. Chem.* **2005**, *77*, 6864.
- Nichkova, M.; Dosev, D.; Perron, R.; Gee, S.; Hammock, B.; Kennedy, I. *Anal. Bioanal. Chem.* **2006**, *384*, 631.
- Lechevallier, S. v.; Lecante, P.; Mauricot, R.; Dexpert, H.; Dexpert-Ghys, J.; Kong, H.-K.; Law, G.-L.; Wong, K.-L. *Chem. Mater.* **2010**, *22*, 6153.
- Das, G. K.; Tan, T. T. Y. *J. Phys. Chem. C* **2008**, *112*, 11211.
- Glaspell, G.; Anderson, J.; Wilkins, J. R.; El-Shall, M. S. *J. Phys. Chem. C* **2008**, *112*, 11527.
- Dosev, D.; Nichkova, M.; Dumas, R. K.; Gee, S. J.; Hammock, B. D.; Liu, K.; Kennedy, I. M. *Nanotechnology* **2007**, *18*, 055102.
- Liu, G. K.; Chen, X. Y.; Zhuang, H. Z.; Li, S.; Niedbalab, R. S. *J. Solid. State. Chem.* **2003**, *171*, 123.
- Mialon, G.; Türkcan, S.; Alexandrou, A.; Gacoin, T.; Boilot, J. P. *J. Phys. Chem. C* **2009**, *113*, 18699.
- Dai, Q.; Song, H.; Wang, M.; Bai, X.; Dong, B.; Qin, R.; Qu, X.; Zhang, H. *J. Phys. Chem. C* **2008**, *112*, 19399.
- Yang, J.; Li, C. X.; Cheng, Z. Y.; Zhang, X. M.; Quan, Z. W.; Zhang, C. M.; Lin, J. J. *Phys. Chem. C* **2007**, *111*, 18148.
- Tissue, B. M. *Chem. Mater.* **1998**, *10*, 2837.
- Macedo, A. G.; Ferreira, R. A. S.; Ananias, D.; Reis, M. S.; Amaral, V. S.; Carlos, L. D.; Rocha, J. *Adv. Funct. Mater.* **2010**, *20*, 624.
- Liu, L. Q.; Ma, E.; Li, R. F.; Liu, G. K.; Chen, X. Y. *Nanotechnology* **2007**, *18*, 015403.
- Meltzer, R. S.; Feofilov, S. P.; Tissue, B.; Yuan, H. B. *Phys. Rev. B* **1999**, *60*, R14012.
- Meltzer, R. S.; Yen, W. M.; Zheng, H.; Feofilov, S. P.; Dejneka, M. J.; Tissue, B.; Yuan, H. B. *J. Lumin.* **2001**, *94–95*, 217.
- Schniepp, H.; Sandoghdar, V. *Phys. Rev. Lett.* **2002**, *89*, 257403.
- Dolgaleva, K.; Boyd, R. W.; Milonni, P. W. *J. Opt. Soc. Am. B.* **2007**, *24*, 516.
- Duan, C.-K.; Reid, M. F.; Wang, Z. *Phys. Lett. A* **2005**, *343*, 474.
- Heber, J.; Hellwege, K. H.; Köbler, U.; Murmann, H. *Z. Phys.* **1970**, *237*, 189.
- Buijs, M.; Meyerink, A.; Blasse, G. *J. Lumin.* **1987**, *37*, 9.
- Gordon, W. O.; Carter, J. A.; Tissue, B. M. *J. Lumin.* **2004**, *108*, 339.
- Bihari, B.; Eilers, H.; Tissue, B. M. *J. Lumin.* **1997**, *75*, 1.
- Guixia, L.; Guangyan, H.; Jinxian, W.; Xiangting, D. *J. Alloys. Compd.* **2007**, *432*, 200.
- Liu, L. Q.; Chen, X. Y. *Nanotechnology* **2007**, *18*, 255704.
- Liu, L.; Ma, E.; Li, R.; Chen, X. *J. Nanosci. Nanotechnol.* **2008**, *8*, 1398.
- Pires, A. M.; Santos, M. F.; Davolos, M. R.; Stucchi, E. B. *J. Alloys. Compd.* **2002**, *344*, 276.
- Li, Y.; Hong, G. *J. Lumin.* **2007**, *124*, 297.
- Jia, G.; Liu, K.; Zheng, Y. H.; Song, Y. H.; Yang, M.; You, H. P. *J. Phys. Chem. C* **2009**, *113*, 6050.
- Choi, J.; Tseng, T.-K.; Davidson, M.; Holloway, P. H. *J. Mater. Chem.* **2011**, *21*, 3113.
- Bai, X.; Song, H.; Yu, L.; Yang, L.; Liu, Z.; Pan, G.; Lu, S.; Ren, X.; Lei, Y.; Fan, L. *J. Phys. Chem. B* **2005**, *109*, 15236.
- Buijs, M.; Blasse, G. *J. Sol. Stat. Chem.* **1987**, *71*, 296.
- Riseberg, L. A.; Moos, H. W. *Phys. Rev. B.* **1968**, *174*, 429.
- Miyakawa, T.; Dexter, D. L. *Phys. Rev. B.* **1970**, *1*, 2961.
- Zych, E. *J. Phys.: Condens. Matter* **2002**, *14*, 5637.
- Hunt, R. B.; Pappalardo, R. G. *J. Lumin.* **1985**, *34*, 133.
- Wuister, S. F.; Donega, C. D.; Meijerink, A. *J. Chem. Phys.* **2004**, *121*, 4310.